Robustness of superconductivity to structural disorder in $Sr_{0.3}(NH_2)_y(NH_3)_{1-y}Fe_2Se_2$

F. R. Foronda,[1,*] S. Ghannadzadeh,[1,2] S. J. Sedlmaier,[3] J. D. Wright,[1] K. Burns,[3] S. J. Cassidy,[3,4] P. A. Goddard,[5] T. Lancaster,[6] S. J. Clarke,[3] and S. J. Blundell[1,†]

[1]*Oxford University Department of Physics, Clarendon Laboratory, Parks Road, Oxford OX1 3PU, United Kingdom*
[2]*High Field Magnet Laboratory, Institute for Molecules and Materials, Radboud University, 6525 ED Nijmegen, The Netherlands*
[3]*Department of Chemistry, University of Oxford, Inorganic Chemistry Laboratory, South Parks Road, Oxford OX1 3QR, United Kingdom*
[4]*Diamond Light Source Ltd., Harwell Science and Innovation Campus, Didcot OX11 0DE, United Kingdom*
[5]*Department of Physics, University of Warwick, Gibbet Hill Road, Coventry CV4 7AL, United Kingdom*
[6]*Durham University, Centre for Materials Physics, South Road, Durham DH1 3LE, United Kingdom*

(Received 15 July 2015; published 20 October 2015)

The superconducting properties of a recently discovered high-T_c superconductor, Sr/ammonia-intercalated FeSe, have been measured using pulsed magnetic fields down to 4.2 K and muon spin spectroscopy down to 1.5 K. This compound exhibits intrinsic disorder resulting from random stacking of the FeSe layers along the c axis that is not present in other intercalates of the same family. This arises because the coordination requirements of the intercalated Sr and ammonia moieties imply that the interlayer stacking (along c) involves a translation of either $\mathbf{a}/2$ or $\mathbf{b}/2$ that locally breaks tetragonal symmetry. The result of this stacking arrangement is that the Fe ions in this compound describe a body-centered-tetragonal lattice in contrast to the primitive arrangement of Fe ions described in all other Fe-based superconductors. In pulsed magnetic fields, the upper critical field H_{c2} was found to increase on cooling with an upward curvature that is commonly seen in type-II superconductors of a multiband nature. Fitting the data to a two-band model and extrapolation to absolute zero gave a maximum upper critical field $\mu_0 H_{c2}(0)$ of 33(2) T. A clear superconducting transition with a diamagnetic shift was also observed in transverse-field muon measurements at $T_c \approx 36.3(2)$ K. These results demonstrate that robust superconductivity in these intercalated FeSe systems does not rely on perfect structural coherence along the c axis.

DOI: 10.1103/PhysRevB.92.134517 PACS number(s): 76.75.+i, 74.25.Dw, 74.25.N−, 74.70.Xa

I. INTRODUCTION

The discovery of superconductivity in iron-based materials [1] has led to a new family of systems with substantial structural variations, but all compounds are composed of FeB layers (where B = As,Se,Te,P or some mixture) and the variations arise from the way these layers are assembled and which atoms are included between them [2–5]. Increasing the interlayer separation in FeSe has been found to give rise to a dramatic effect on the superconducting transition temperature T_c. For example, pure FeSe (T_c = 8.5 K [6]) can be intercalated with alkali-metal ions and ammonia [7–9] or other organic molecules [7,10] to produce new superconductors with transition temperatures of up to around 45 K. Similar high-T_c behavior can be induced using metal hydroxides as the spacer layer [11–14]. This trend of increase in T_c with increasing layer separation does not continue indefinitely [10], and this effect can be rationalized through first-principles calculations [15]. However, the effect of controlled structural disorder on T_c has not been so closely examined. We have identified an intercalated FeSe compound in which random stacking of well-defined layers results in a paracrystalline structure. In this paper, we demonstrate that the superconducting state is nevertheless robust.

The compound $Sr_x(NH_2)_y(NH_3)_{1-y}Fe_2Se_2$ ($x = 0.3$, $0.2 \leqslant y \leqslant 0.6$) belongs to a family of layered intercalates $A_x(NH_2)_y(NH_2)_{1-y}Fe_2Se_2$ (A = Li, Na, K, Rb, Cs, Ca, Sr, Ba, Eu, and Yb). In these materials, bulk superconductivity occurs in anti-PbO-type FeSe layers composed of edge-sharing $FeSe_4$ tetrahedra that are separated by metal ions, amide ions, and ammonia molecules [8,9,16,17]. Figure 1 shows the various structures and the conventional unit cell with $a = b \approx 3.8$ Å and $c = 16.5$–17.4 Å. These compounds remain tetragonal down to low temperatures and do not exhibit an orthorhombic distortion. Neutron scattering and x-ray-diffraction measurements have revealed some structural differences related to the size of the cation used; when it is small (A = Li), Fe ions in adjacent layers occupy the same primitive tetragonal sublattice [8], as shown in Fig. 1(a). For larger cations (A = K,Rb), the arrangement of Fe and Se ions is unchanged, but the larger electropositive cations share the same sites as the amide and ammonia moieties in the body-centered position of the primitive Fe sublattice [see Fig. 1(b)]. As we describe in detail in Sec. III, the Sr case presents a scenario in which the coordination requirements of the Sr cation and the amide or ammonia moieties are best satisfied by an arrangement of adjacent FeSe layers that results in a random stacking of these layers along the c axis, which may be described as paracrystalline. We will demonstrate through SQUID magnetometry, pulsed magnetic fields, and muon spin rotation (μSR) measurements that, despite this unusual structural disorder, superconductivity remains robust with a $T_c \approx 36$ K that is significantly higher than that of a parent compound.

II. SYNTHESIS

In an argon-filled glove box, finely ground FeSe powder (1.970 g, 14.611 mmol) synthesized from the elements as described elsewhere [8] and pieces of strontium metal (0.640 g,

*francesca.foronda@physics.ox.ac.uk
†s.blundell@physics.ox.ac.uk

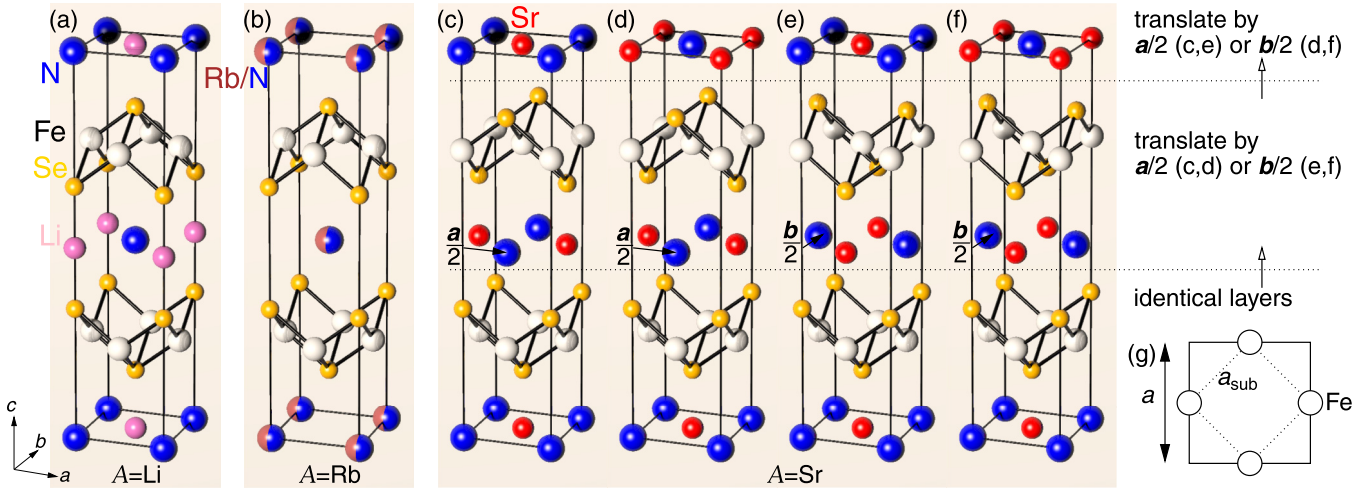

FIG. 1. (Color online) Crystal structure of the FeSe intercalate family in which the spacer layer consists of ammonia with (a) Li, (b) Rb, or (c)–(f) Sr atoms (hydrogen omitted for clarity). In the Li and Rb intercalates, the Fe atoms (gray spheres) in adjacent layers occupy a primitive $a_{sub} \times a_{sub} \times c_{sub}$ sublattice, where $c_{sub} = c/2$ is the distance between adjacent Fe layers (~8.3 Å for the Li intercalate). In the Rb case, the metal ions and ammonia molecules share the same site with 50% occupancy (split pink/blue spheres). In the Sr case, the Fe sublattice is a body-centered-tetragonal unit cell that is elongated by a factor of 2 in the c direction, and the structure contains random stacking faults. The stacking faults are illustrated in (c)–(f) as follows. The dotted lines represent where the stacking faults occur, with the section below the lower dotted line being identical in all four diagrams. Above the lower dotted line, the Fe-Se units are translated relative to those in the lower layer by half a unit cell along either the a or b direction. At the upper dotted line, the same translation along a or b occurs again, so that with n dotted lines there would be 2^n possible configurations. With the two dotted lines shown, (c)–(f) demonstrate the four possible stacking combinations when starting from an identical base layer. The position of the Fe sublattice relative to the unit cell in a single layer, as viewed along the c axis, is shown in (g).

7.304 mmol, ALFA) were placed in a thick-walled glass Schlenk tube capable of withstanding an internal pressure of over 15 bar. The tube was evacuated and cooled to −78 °C with an isopropanol/dry ice cooling bath. While cold, around 50 mL of liquid ammonia was condensed into the Schlenk tube, and the Sr metal was dissolved in the liquid ammonia to produce a blue solution. The valve on the Schlenk tube was closed, isolating it from the line, and the reaction mixture was allowed to warm to room temperature and stirred for 24 h. After the reaction, it was cooled to −78 °C again, allowing the valve to the line to be opened and the ammonia to evaporate off via a mercury-filled bubbler while letting the Schlenk tube slowly warm to room temperature. At the end of this process, the Schlenk tube was placed under dynamic vacuum for 2 min and brought into the glove box. The product was isolated as a very fine black powder. Samples were prepared using both normal and deuterated ammonia. For further measurements, the samples were handled under an inert gas atmosphere at all times.

III. STRUCTURAL CHARACTERIZATION

The crystal structures of the products were analyzed using synchrotron x-ray powder diffraction on beamline I11 at the Diamond Light Source, or beamline ID31 at the ESRF. Samples were sealed under an argon atmosphere within 0.5-mm-diam borosilicate glass capillaries. The diffractograms revealed a series of extremely sharp reflections that could all be indexed on a body-centered-tetragonal unit cell with lattice parameters $a_{sub} = 2.7$ Å and $c = 17.4$ Å [see Fig. 2(a)]. The intensities of these reflections were accounted for by the model shown in Figs. 2(b) and 2(c) in which the familiar square planar Fe nets found in all the iron selenide superconductors with Fe-Fe $= a_{sub} \sim 2.7$ Å are related by the body-centering translation.

Since in this model the basal lattice parameter a_{sub} was equal to the Fe-Fe distance, the selenide ions were inevitably modeled as disordered over two sites located above and below the centers of each square of Fe ions. Further sites were located in the interlamellar space, and they were occupied by N atoms from ammonia or amide moieties (N:Fe ratio 1:2) and Sr ions (Sr:Fe ratio 0.3:2). This model was also obtained using a charge flipping algorithm implemented within TOPAS ACADEMIC [18], and it was consistent for all the samples investigated. The interatomic distances and the coordination environments using this model were chemically realistic providing that local ordering of occupied and unoccupied Se, N, and Sr sites was imposed. This required an $a = b = \sqrt{2}a_{sub}$ basal expansion of the tetragonal unit cell to achieve a chemically realistic FeSe layer and stacking disorder along c to account for the apparent smaller cell.

Weak structured diffuse scattering was evident in the diffractograms as a result of the stacking disorder. This diffuse scattering was accounted for in a semiquantitative manner by constructing a superstructure in which layers were stacked along the c axis in a way that respected the coordination environments for the intercalate species shown in Figs. 1(a) and 1(b). NH_3 and NH_2^- moieties were sixfold-coordinated by selenide ions [a square of four in one layer and a pair in the layer above, producing an isosceles triangular prism; see Fig. 2(g)] such that N-H$\cdots$Se distances were 3.7 Å, similar to those found in the analogous Li/NH_3 intercalates. Sr^{2+} ions were coordinated by a triangle of selenide ions about 3.2 Å apart and by N atoms from the amide or ammonia species

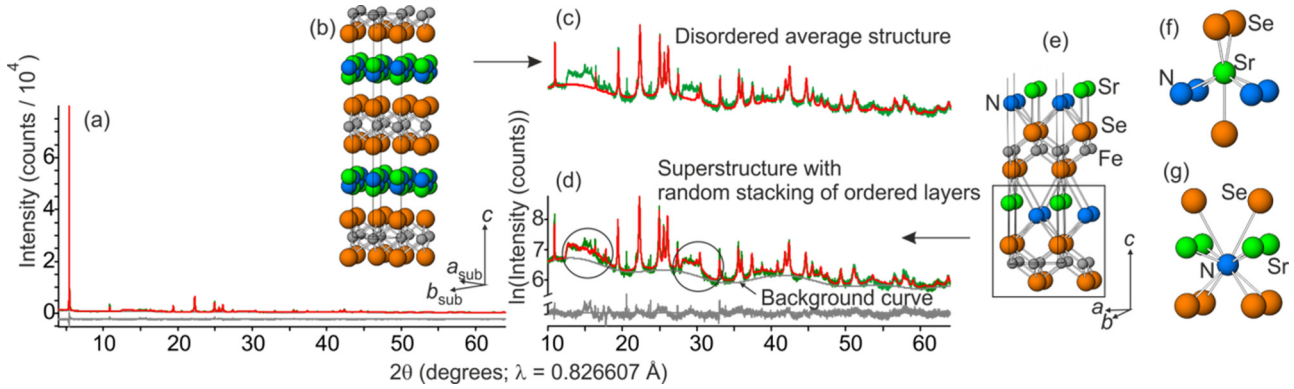

FIG. 2. (Color online) Refinements against I11 powder diffraction data showing experimental (green) and calculated (red line) patterns as well as the difference (gray line). The full pattern is shown in (a) with magnifications of the diffractogram showing calculations from two different models in (c) and (d) [magnifications are shown with the same horizontal scale as (a) but with a logarithmic intensity scale to emphasize the weak features in the data]. The full pattern is dominated by sharp Bragg reflections that can be accounted for by the disordered average structure shown in (b) with space group *I4/mmm* with unit cell $a_{sub} \times a_{sub} \times c$. This model assumes full occupancy of the Fe sites that describe a body-centered-tetragonal unit lattice, but 50% occupancy of the selenide sites and also partial occupancy of the N and Sr sites. However, it fails to account for regions of diffuse scattering, as shown in (c). Part (d) shows an improved fit to the diffuse scattering (ringed) when using a model in which chemically realistic layers [boxed region in diagram (e)] with basal lattice parameters $a = b = \sqrt{2} \times a_{sub}$ are translated by either $a/2$ or $b/2$ relative to their neighbors, as described in the text and Fig. 1. Both fits employed the same background function. Hydrogen atoms attached to the nitrogen atoms were not modeled, but assumed to be directed toward the selenide ions as described in related systems [8]. Parts (f) and (g) show the local coordination environments around Sr and N, respectively.

2.9 Å apart [see Fig. 2(f)]. To achieve these coordination environments, adjacent iron selenide layers were constrained to be translated relative to one another by $a/2$ or $b/2$. A model with a superstructure extending along the c direction composed of 240 layers stacked randomly according to the chemical constraints captured the key features of the diffuse scattering [see Figs. 2(d) and 2(e)], although some discrepancies remain in quantitatively modeling the intensity distribution in these parts of the diffraction pattern. Attempts to explore the diffuse scattering in more detail using transmission electron microscopy were unsuccessful due to the decomposition of these samples in the electron beam. This description of the structure in which well-defined layers are stacked in a disordered manner may be described as paracrystalline [19]. The refinements produced a Sr:Fe ratio of 0.15:1 and an N:Fe ratio of 0.5:1. The measurements conducted so far do not allow the N:H ratio to be determined with certainty, so we use the formula $Sr_{0.3}(NH_2)_y(NH_3)_{1-y}Fe_2Se_2$. Since the Sr/ammonia solution is reducing, the upper bound on y is 0.6, yielding an Fe oxidation state of +2. An Fe oxidation state of +1.8, which is found for other iron selenide systems, would require $y = 0.2$. In what follows, we refer to the mixture of amide and ammonia moieties as NH_z ($2.4 < z < 2.8$).

The key difference between this intercalate and the previously described intercalates containing alkali-metal or alkaline-earth metal ions and ammonia molecules and/or amide ions is that the square arrangement of iron atoms in one layer is related to that in the neighboring layers by a basal plane translation of half a unit cell in either the a or b direction, resulting in the $2.7 \times 2.7 \times 17.4$ Å^3 body-centered-tetragonal arrangement of Fe atoms [see Figs. 1(c)–1(f)]. This is in contrast to the arrangement of Fe atoms in all other iron-based superconductors in which the Fe atoms in two adjacent layers are related by the $c/2$ lattice vector and thus describe a primitive $2.7 \times 2.7 \times c_{sub}$ sublattice. Figures 1(c)–1(f) demonstrate how the nature of these translations, represented by dotted lines, results in a paracrystalline structure as follows. Consider starting from an identical base layer (the region below the first dotted line), in which the Fe, Se, and intercalated species occupy the same crystallographic sites as those found in the Li case. To construct the next layer, each atom must be translated by either $a/2$ or $b/2$. In each case, the Fe sites are the same but the positions of the Se, ammonia, and metal species change depending on the chosen direction. As the translation occurs along a randomly chosen direction with the addition of each layer, it follows that for n layers there would be 2^n possible configurations. Our interpretation of the structural data is that despite the random stacking, the well-separated FeSe layers themselves remain well ordered, and this helps to explain our findings, described below, that robust superconductivity is preserved in these systems.

IV. SQUID MAGNETOMETRY

Magnetic susceptibility measurements were recorded using a Quantum Design MPMS-XL superconducting quantum interference device (SQUID) magnetometer. Samples of the Sr/NH_z intercalate (30.2 and 29.8 mg) and the Sr/ND_z intercalate (34.0 and 30.2 mg) were filled and immobilized in gelatin capsules. Measurements were conducted in dc fields of 5 mT in the temperature range 2–150 K after cooling in zero applied field (ZFC) and in the measuring field (FC).

The magnetometry measurements performed directly after the synthesis (Fig. 3) indicate bulk superconductivity with a noticeable sharp drop to negative susceptibility values at $T_c = 36(1)$ K. There is no effect of H/D substitution on T_c. Although the superconducting volume fraction is larger in the case of D, we believe this is consistent with the natural variability of volume fractions achieved in different syntheses.

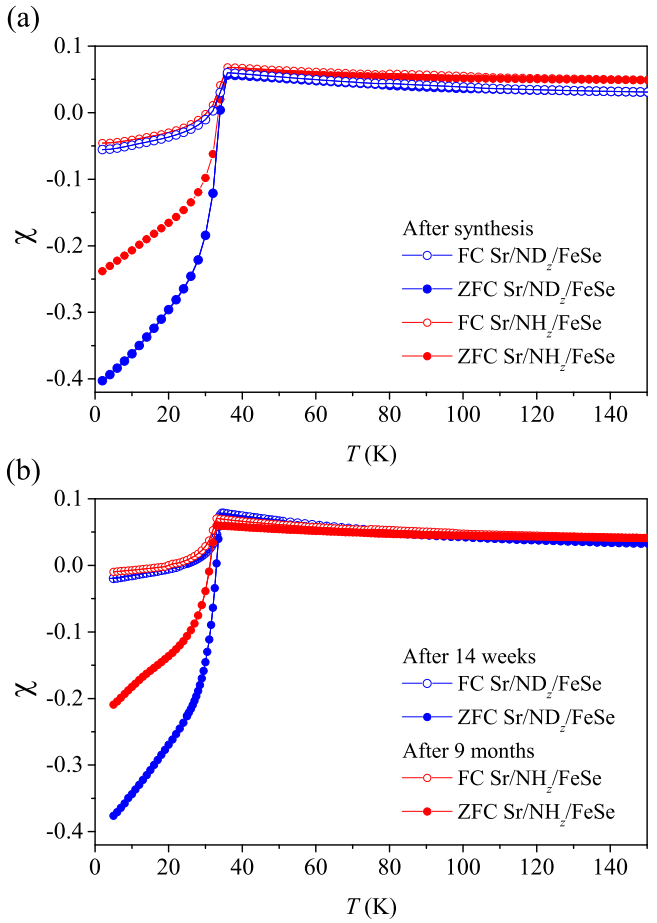

FIG. 3. (Color online) (a) Volume susceptibility χ of Sr/ND$_z$ and Sr/NH$_z$ intercalated iron selenide after synthesis. (b) Measurements showing a slight decrease of T_c after 14 weeks and 9 months for the Sr/ND$_z$ and the Sr/NH$_z$ intercalate, respectively.

Even after nine months, the superconducting volume fractions and the sharp drop at T_c were found to be unchanged. A small reduction in T_c (of 2–3 K) was detected, although this was not found to be correlated with any significant change in structure. For the remainder of the paper, we will present magnetometry and μSR data on the Sr/NH$_z$ intercalate.

V. PULSED-FIELD MAGNETOMETRY

Powder samples were measured at the Nicholas Kurti Magnetic Field Laboratory, Oxford using a proximity detector oscillator (PDO) dynamic susceptometer [20,21]. The sample is mounted in an ampoule under an argon atmosphere and placed inside a small sensor coil that is inductively coupled to the PDO circuit. This is essentially an LCR circuit with a resonant frequency f that is measured as a function of field and temperature. In metals (superconductors) f is highly dependent on changes in the skin (penetration depth), and in insulators the signal is dominated by the magnetic permeability. Thus when sweeping in field or temperature, the superconducting phase transition manifests as a large change of f at H_{c2} or T_c, which corresponds to the difference in skin and penetration depth of the two states.

Data were taken for temperatures in the range 4.2–40 K in fields of up to 38 T. Below T_c, the onset of superconductivity is marked by a sudden rise in frequency and a deviation from the normal-state signal [see Fig. 4(a)]. Additional heating can occur due to eddy currents that are generated in the mixed or normal state by the applied field. In some cases, this produces hysteresis in the data and a shift in H_{c2}, with the effect being more pronounced with a larger dB/dt (a shorter pulse length for the same maximum field). We find our samples to be insensitive to these effects and observe no difference in f at varying pulse lengths between 7 and 14 ms [see Fig. 4(c) for field profiles of the pulses].

We note that due to the broadness of the phase transition, the value of H_{c2} is particularly difficult to determine at low T. This may be due to the critical field anisotropy between the in-plane and out-of-plane directions increasing as the system is cooled, and so for a powdered sample there is a more gradual change in frequency. Thus, we define two different methods for extracting H_{c2}. First, we take H_{c2} as the peak in d^2f/dH^2 and its uncertainty as the half-width at half-maximum [see Fig. 4(d)]. Second, one may perform a linear extrapolation of the curve on either side of the transition and define H_{c2} as the point of intersection of these two slopes. In this case, another criterion is the point at which the line extrapolated from the curve below the critical field crosses the normal-state signal. We take the uncertainty as the difference between these two points of intersection [see Fig. 4(b)]. We find that both methods give similar results, with H_{c2} increasing steadily as the sample is cooled (see Fig. 8). We note that the curve exhibits a concave form that has been observed in multiband high-T_c superconductors [22].

VI. TRANSVERSE FIELD μSR MEASUREMENTS

To probe the internal field distribution in the vortex state, transverse field μSR (TF μSR) measurements were carried out using the GPS instrument at the Swiss Muon Source (PSI), Switzerland and the MuSR spectrometer at ISIS, UK. In these measurements, spin-polarized muons are implanted into the material with an external field B_{app} applied perpendicular to the initial muon spin direction. They will then rotate at the Larmor frequency $\omega = \gamma_\mu B_{loc}$, where $\gamma_\mu/2\pi = 135.5$ MHz T^{-1} is the muon gyromagnetic ratio and B_{loc} is the local field, which may include contributions from B_{app}, magnetic ions, and nuclear dipoles. This is measured directly by the time-dependent positron decay asymmetry $A(t)$ [23].

Muons implanted in a type-II superconductor will settle in particular crystallographic sites and experience a magnetic field due to the applied field as well as any internal variation resulting from the formation of a vortex lattice. However, as the vortex lattice is, in general, incommensurate with the crystal lattice, the full range of the field distribution within the vortex lattice is sampled, although it is broadened slightly by the field from nuclear spins. In TF measurements, the measured asymmetry is proportional to the spin polarization as measured by individual detector banks. This experimental situation can be modeled using a fit function,

$$A(t) = A_{bg}\cos(\gamma B_{app}t + \phi)\exp[-(\sigma_{bg}t)^2/2] + A_{VL}\cos(\gamma B_{pk}t + \phi)\exp[-(\sigma_{VL}t)^2/2], \quad (1)$$

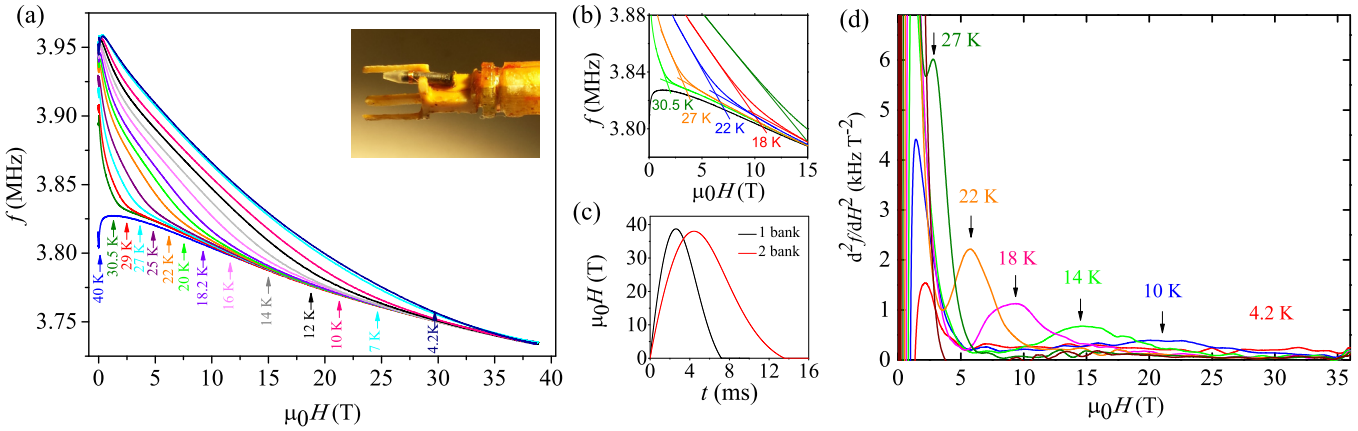

FIG. 4. (Color online) (a) Down-sweep portion of pulsed magnetic field data for $Sr_{0.3}(NH_2)_y(NH_3)_{1-y}Fe_2Se_2$ at various temperatures $T \leqslant 40$ K. Data are offset so that the frequency in the normal state matches that measured at 40 K (blue line). Inset: sample mounted on the end of the PDO probe before lowering into a cryostat. (b) Close-up showing the intersection of two slopes used to determine H_{c2}. (c) Typical 38 T field pulses demonstrate how dB/dt varies with pulse length when using one or two banks of charging capacitors, each providing an energy of up to 0.2 MJ. (d) Second method for calculating H_{c2} as the peak position in d^2f/dH^2.

where the phase ϕ results from the detector geometry, and A_{VL} and A_{bg} are the relaxing asymmetry due to vortex lattice and background contributions, respectively (the latter originates from muons stopping in the nonsuperconducting fraction of the sample or silver sample holder). This model assumes a symmetric Gaussian distribution of local fields with a peak value B_{pk} (B_{app}) and standard deviation, or damping factor, σ_{VL} (σ_{bg}) corresponding to the vortex lattice (background) contributions. The width of the field distribution is given by $B_{rms} = \sigma_{VL}/\gamma_\mu$ and its temperature dependence is shown in Fig. 5. We observe a broadening of the field distribution (increase in B_{rms}) when the sample is cooled through T_c in an applied field of 10 mT that can be attributed to the formation of the vortex lattice with superconductivity setting in at around 36.3(2) K. As the material enters the superconducting state, the applied field is partially screened causing a diamagnetic shift in B_{pk} for $T < T_c$. For powdered samples of anisotropic superconductors such as these, the in-plane penetration depth λ_{ab} is related to the field width via

$$B_0 = \frac{\sqrt{0.00371}\Phi_0}{\left(3^{\frac{1}{4}}\lambda_{ab}\right)^2}, \tag{2}$$

where Φ_0 is a magnetic flux quantum and B_0 is the vortex lattice contribution to B_{rms} [24]. For these data, it is assumed that the only other contribution to B_{rms} is from nuclear dipole fields, which are temperature-independent and add in quadrature. We fit our data to the phenomenological functions

$$B_{rms}(T) = \left\{B_0^2\left[1-\left(\frac{T}{T_c}\right)^{\alpha}\right]^{2\beta} + B_{dip}^2\right\}^{\frac{1}{2}}, \tag{3}$$

$$B_{pk}(T) = B_{app} - B_{dia}\left[1-\left(\frac{T}{T_c}\right)^{\alpha'}\right]^{\beta'}, \tag{4}$$

where B_{dia} is the maximum diamagnetic shift of the peak field, and B_0 and B_{dip} are the widths corresponding to the vortex lattice (at $T = 0$) and nuclear dipole contributions, respectively. For the fits shown in Fig. 5, the fitted parameters are $\beta = 0.33(3)$ and $\beta' = 0.43(3)$ with fixed $\alpha = \alpha' = 1$. Using a weighted average between the extracted value of B_0 of these data and additional measurements on a second batch of sample, we calculate a penetration depth of $\lambda_{ab}(T = 0) = 292(3)$ nm.

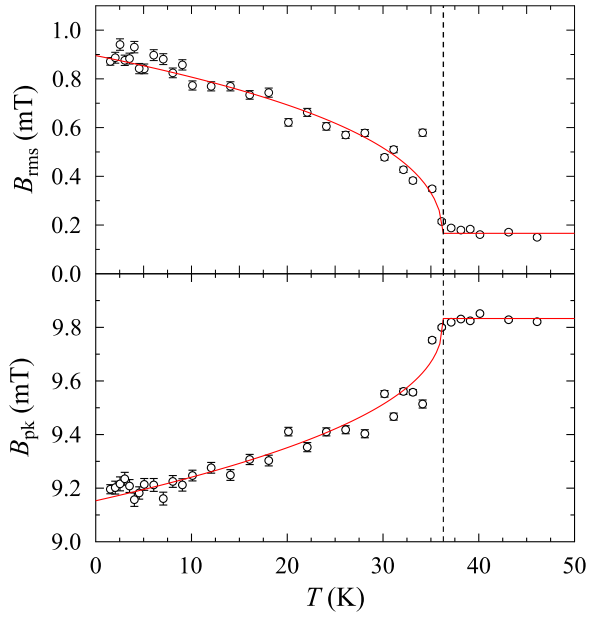

FIG. 5. (Color online) Temperature dependences of field width B_{rms} and peak field B_{pk} from TF μSR measurements made on the MuSR spectrometer. Fits (red lines) are to Eqs. (3) and (4) with the former used to extract absolute values of $B_{rms}(T = 0)$ and $\lambda_{ab}(T = 0)$.

VII. ZERO-FIELD AND LONGITUDINAL-FIELD μSR MEASUREMENTS

Zero-field measurements (ZF μSR) were used to further probe the intrinsic magnetism of the system. No spontaneous oscillations were observed in the forward-backward asymmetry across the whole temperature range, nor was there any discontinuous change in amplitudes or recovery of the baseline

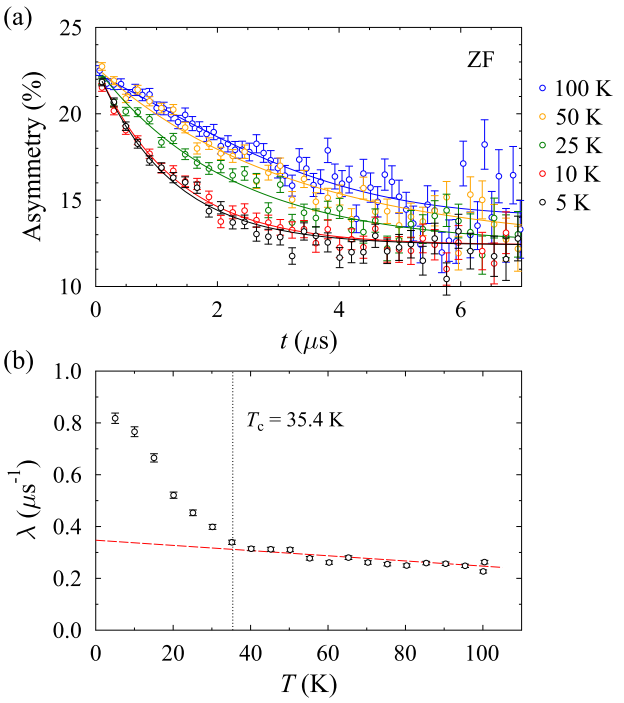

FIG. 6. (Color online) (a) Example asymmetry spectra from ZF μSR measurements taken on the GPS spectrometer. Fits are to Eq. (5). (b) Temperature dependence of relaxation rate λ measured in zero field. Below T_c the data points deviate sharply from the linear trend (red line).

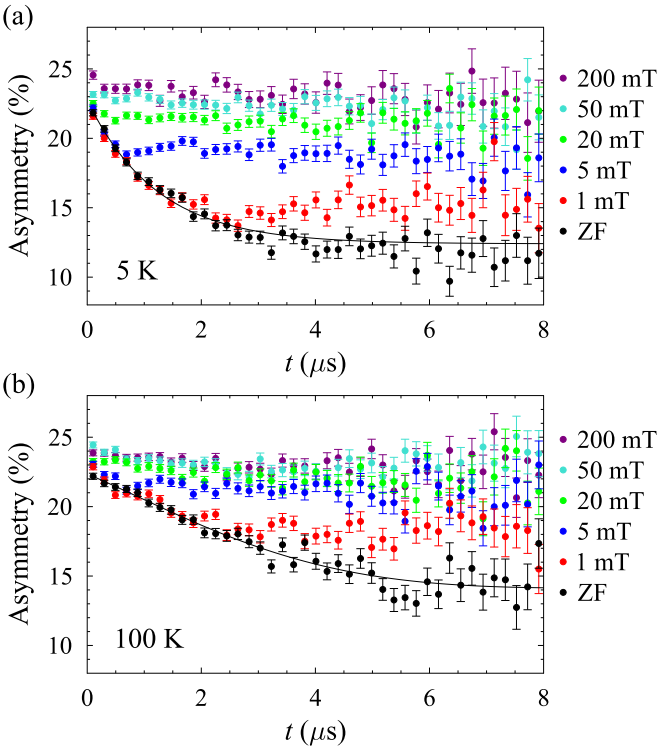

FIG. 7. (Color online) Example LF μSR spectra at (a) 5 K and (b) 100 K. Above T_c the spins are decoupled at relatively low fields ($\approx$5 mT).

asymmetry at low temperatures [see Fig. 6(a)]. Together these make the presence of any long-range magnetic order unlikely. Given that the spectra do not follow a Kubo-Toyabe relaxation, it is also unlikely that the relaxation is caused solely by nuclear moments. The lack of recovery of the baseline asymmetry at late times suggests dynamic fluctuations, and we therefore attribute the ZF signal to relaxation caused by disordered, fluctuating electronic moments. The data were fitted to the function

$$A(t) = A_{\mathrm{rel}} \exp(-\lambda t) + A_{\mathrm{base}}, \tag{5}$$

where A_{rel} is the relaxing asymmetry with relaxation rate λ, and A_{base} is a nonrelaxing background. A_{rel} can be considered as the lower bound for the superconducting volume fraction, which for this sample was around 1/3. Exponential relaxation often describes dense spin systems that are dynamically fluctuating, where the relaxation rate λ is proportional to the variance of the local magnetic field distribution and also to the fluctuation time, or a dilute spin systems in the presence of dynamic fluctuations. Upon cooling, the relaxation rate λ [Fig. 6(b)] is seen to increase slowly with decreasing temperature. However, below superconducting T_c it increases far more rapidly, suggesting that the relaxation rate is in some way coupled to the superconducting order parameter.

Longitudinal field measurements (LF μSR) were made at 5 and 100 K in which a field was applied in the initial direction of the muon polarization (see Fig. 7). For data measured at 5 K [Fig. 7(a)], the sample was cooled below T_c in zero applied field. At both temperatures, the relaxation is decoupled at relatively low fields ($\approx$5 mT at 100 K and $\approx$20 mT at 5 K), suggesting that the relaxation is due to fairly dilute and/or static spins with residual dynamic fluctuations. One scenario is that there is a sizable contribution to the ZF relaxation from static nuclear moments, with dilute, fluctuating electronic moments providing additional relaxation. The lack of any peak in λ suggests the absence of any freezing of the dynamics of the moments (as one would expect in a spin glass due to magnetic interactions), supporting the interpretation that these are dilute and not strongly interacting with each other. The fact that the relaxation rate is coupled to the superconducting order parameter implies that the moments are embedded in the superconductor, rather than in phase-separated pockets. At high temperatures compared to T_c, the moment size and/or fluctuation rate increase slowly upon cooling. Upon cooling below T_c, the muon spins likely experience a combination of slower fluctuation times, larger moments, and an increased width of the field distribution. The latter could arise in a manner analogous to the increase in B_{rms} in the TF measurements. Specifically, if the moments are locally in a normal (rather than superconducting) region and sufficiently numerous that there is a degree of overlap of their magnetic fields in the superconducting regions, then the decreasing penetration depth upon cooling would lead muons, which decorate all of the sample, to experience a broader distribution of local fields. Taken together, the ZF measurements therefore suggest the presence of a small concentration of dilute magnetic moments dispersed in the superconducting volume, but whose presence does not seem to adversely affect the presence of superconductivity.

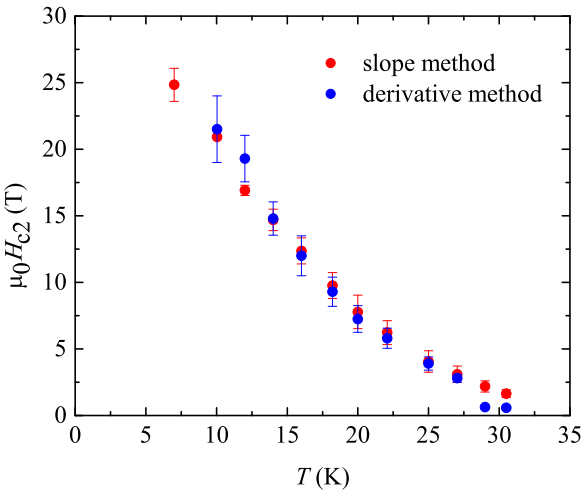

FIG. 8. (Color online) Phase diagram for $Sr_{0.3}(NH_2)_y(NH_3)_{1-y}Fe_2Se_2$ using the slope and derivative methods as described in the text. The transition is too broad for a reliable estimate of H_{c2} at 4.2 K.

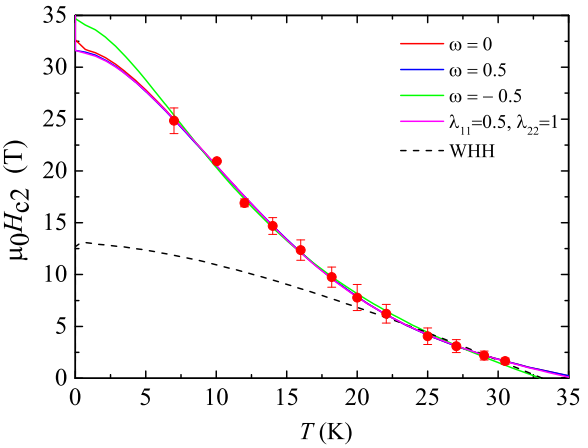

FIG. 9. (Color online) Fits of H_{c2} using the two-band Gurevich model [Eq. (6)] with either a fixed ω or fixed intraband coupling constants λ_{11} and λ_{22} (H_{c2} determined by the slope method). The dotted line shows a fit to the single-band WHH model.

VIII. DISCUSSION

Pulsed-field measurements indicate an upward curvature in H_{c2} versus temperature (see Fig. 8), which may be indicative of a multiband nature. This type of behavior has been observed in other layered two-band superconductors such as the FeAs-based systems [25,26] and the parent compound FeSe using resistivity measurements [27]. Fits of the Werthamer-Helfand-Hohenberg (WHH) model [28] for a one-band superconductor in the dirty limit did not converge. Instead, we use a model developed by Gurevich that is based on a weakly coupled two-band BCS superconductor [29,30]. This includes scattering from nonmagnetic impurities, orbital pair breaking, strong electron-phonon coupling, and spin paramagnetism (note that unlike the WHH model, it does not account for spin-orbit effects). The model parameters are the band diffusivities D_1 and D_2 and the intraband (λ_{11} and λ_{22}) and interband (λ_{12} and λ_{21}) coupling constants. Assuming that the nonmagnetic impurity scattering does not affect T_c, the upper critical field is given in reduced natural units $h = H_{c2}D_1/2\phi_0 T$ and $t = T/T_c$ by

$$a_0[\ln t + U(h)][\ln t + U(\eta h)] + a_2[\ln t + U(\eta h)] + a_1[\ln t + U(h)] = 0, \quad (6)$$

where

$$U(x) = \psi\left(\frac{1}{2} + x + i\frac{\mu_B H}{2\pi T}\right) - \psi(x), \quad (7)$$

in which $\psi(x)$ is the digamma function, $\eta = D_2/D_1$ is the ratio of band diffusivities, and the constants a_0, a_1, and a_2 are functions of the coupling constants.

In any case, the model is difficult to fit due to over-parametrization; at high temperatures, H_{c2} is strongly dependent on D_2/D_1 and weakly dependent on the coupling constants, which contribute significantly only in the mK temperature range. Consequently, fits to the data converge only when one set of coupling constants (either interband or intraband) are fixed. Fits are shown in Fig. 9 for various values of λ_{11}, λ_{22}, and $w = \lambda_{11}\lambda_{22} - \lambda_{12}\lambda_{21}$. The Gurevich model was successful in modeling the upward curvature of H_{c2}, which stems from the difference in diffusivities of the two bands, i.e., $\frac{D_2}{D_1} < 1$ [30]. However, we found that it was possible to fit for both a strong (when $w < 0$) and weak ($w > 0$) interband coupling, and fitted parameters varied considerably depending on the values of the chosen coupling constants and the method for finding H_{c2}. This is particularly noticeable when extrapolating $H_{c2}(T)$ to absolute zero. When using H_{c2} values extracted by the slope method as described earlier, we find $\mu_0 H_{c2}(0) \approx 33(2)$ T to be fairly consistent across various different scenarios (see Fig. 9). The derivative method for calculating H_{c2} could not be extended to the lowest-temperature datum and hence it produced a poorly constrained estimate, thus this method was deemed less reliable.

The Uemura relation [31] is a scaling relation between T_c and the superfluid stiffness ρ_s, which seems to hold well for many exotic superconductors [32]. It is known to break down for overdoped cuprates [33] and may be an oversimplification [34], and other scaling relation behaviors have been explored [35–38]. Nevertheless, the Uemura plot of T_c against ρ_s provides a convenient means of exploring the energy scale to break up pairs as a function of the strength of the order parameter, and our TF μSR data allow us to extract an estimate of $\rho_s = c^2/\lambda_{ab}^2$. As shown in Fig. 10, we find that the Sr intercalated compound is close to the main scaling line on the Uemura plot, as is the Li intercalated material [8], and this behavior correlates with underdoped cuprates and many other iron-based superconductors. Note that there is also another, lower line in this plot, which is common to electron-doped cuprates [39,40] and $LiFe_{1-x}Co_xAs$ [41,42]. For those materials, it is found that although the superconducting state is reasonably robust (the superfluid is stiff), the strength of the pairing is significantly suppressed, but these considerations do not seem to apply to our intercalated compounds.

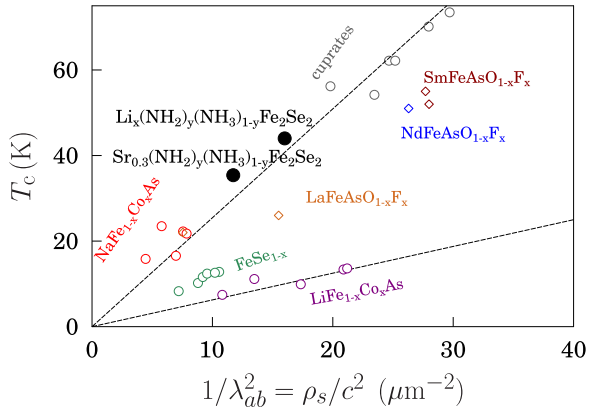

FIG. 10. (Color online) The Uemura plot of T_c against superfluid stiffness $\rho_s = \frac{c^2}{\lambda^2_{ab}}$ shows that the intercalates $A_x(NH_2)_y(NH_3)_{1-y}Fe_2Se_2$ (A = Sr,Li) fall close to the main scaling line.

IX. CONCLUSION

We have probed the superconducting properties of a recently discovered superconductor $Sr_{0.3}(NH_2)_y(NH_3)_{1-y}Fe_2Se_2$ using pulsed-field magnetometry and μSR techniques. The upper critical field was shown to increase upon cooling and exhibited a concave form that is reminiscent of other multigap high-temperature superconductors, which when extrapolated to absolute zero give a maximum upper critical field of $\mu_0 H_{c2}(0) \approx 33(2)$ T. TF μSR measurements show a clear diamagnetic shift and a broadening of the field width that is highly reproducible between different batches of sample, with the onset of superconductivity at 36.3(2) K. ZF μSR did not reveal any long-range magnetic order but dilute electronic moments with some residual dynamics and whose behavior is coupled to the superconducting order parameter. We find that intercalation of Sr atoms together with amide and ammonia introduces intrinsic stacking disorder that results in a paracrystalline state. The system nevertheless retains complete structural order of the Fe sublattice, and thus these results demonstrate that robust superconductivity does not rely on perfect structural coherence along the c axis.

ACKNOWLEDGMENTS

This work was supported by the UK EPSRC via Grant No. EP/I017844. We thank the EPSRC for studentship support for F.R.F. and fellowship support for T.L. We thank the STFC ISIS Facility and Swiss Muon Source, Paul Scherrer Institut for the provision of beam time, and we are grateful for the assistance of A. Amato, P. J. Baker, and instrument scientists on beamline I11 at Diamond. S.J.C. thanks both EPSRC and Diamond for studentship support. S.J.S. acknowledges the support of a DFG Fellowship (SE2324/1-1). We are grateful to J. Hadermann (EMAT, Antwerp) for attempting transmission electron microscopy measurements on these samples.

[1] Y. Kamihara, T. Watanabe, M. Hirano, and H. Hosono, J. Am. Chem. Soc. **130**, 3296 (2008).
[2] J. Paglione and R. L. Greene, Nat. Phys. **6**, 645 (2010).
[3] P. J. Hirschfeld, M. M. Korshunov, and I. I. Mazin, Rep. Prog. Phys. **74**, 124508 (2011).
[4] D. C. Johnston, Adv. Phys. **59**, 803 (2010).
[5] E. Dagotto, Rev. Mod. Phys. **85**, 849 (2013).
[6] T. M. McQueen, Q. Huang, V. Ksenofontov, C. Felser, Q. Xu, H. Zandbergen, Y. S. Hor, J. Allred, A. J. Williams, D. Qu, J. Checkelsky, N. P. Ong, and R. J. Cava, Phys. Rev. B **79**, 014522 (2009).
[7] A. Krzton-Maziopa, E. V. Pomjakushina, V. Y. Pomjakushin, F. von Rohr, A. Schilling, and K. Conder, J. Phys.: Condens. Matter **24**, 382202 (2012).
[8] M. Burrard-Lucas, D. G. Free, S. J. Sedlmaier, J. D. Wright, S. J. Cassidy, Y. Hara, A. J. Corkett, T. Lancaster, P. J. Baker, S. J. Blundell, and S. J. Clarke, Nat. Mater. **12**, 15 (2013).
[9] T. Ying, X. Chen, G. Wang, S. Jin, T. Zhou, X. Lai, H. Zhang, and W. Wang, Sci. Rep. **2**, 426 (2012).
[10] T. Noji, T. Hatakeda, S. Hosono, T. Kawamata, M. Kato, and Y. Koike, Physica C **504**, 8 (2014).
[11] H. Sun, D. N. Woodruff, S. J. Cassidy, G. M. Allcroft, S. J. Sedlmaier, A. L. Thompson, P. A. Bingham, S. D. Forder, S. Cartenet, N. Mary, S. Ramos, F. R. Foronda, B. H. Williams, X. Li, S. J. Blundell, and S. J. Clarke, Inorg. Chem. **54**, 1958 (2015).
[12] U. Pachmayr, F. Nitsche, H. Luetkens, S. Kamusella, F. Brückner, R. Sarkar, H.-H. Klauss, and D. Johrendt, Angew. Chem. Int. Ed. **54**, 293 (2015).
[13] X. F. Lu, N. Z. Wang, H. Wu, Y. P. Wu, D. Zhao, X. Z. Zeng, X. G. Luo, T. Wu, W. Bao, G. H. Zhang, F. Q. Huang, Q. Z. Huang, and X. H. Chen, Nat. Mater. **14**, 325 (2015).
[14] T. Hatakeda, T. Noji, T. Kawamata, M. Kato, and Y. Koike, J. Phys. Soc. Jpn. **82**, 123705 (2013).
[15] D. Guterding, H. O. Jeschke, P. J. Hirschfeld, and R. Valentí, Phys. Rev. B **91**, 041112 (2015).
[16] E.-W. Scheidt, V. Hathwar, D. Schmitz, A. Dunbar, W. Scherer, F. Mayr, V. Tsurkan, J. Deisenhofer, and A. Loidl, Eur. Phys. J. B **85**, 279 (2012).
[17] S. J. Sedlmaier, S. J. Cassidy, R. G. Morris, M. Drakopoulos, C. Reinhard, S. J. Moorhouse, D. O'Hare, P. Manuel, D. Khalyavin, and S. J. Clarke, J. Am. Chem. Soc. **136**, 630 (2014).
[18] A. A. Coelho, J. Appl. Cryst. **36**, 86 (2003).
[19] J. C. Burley, P. D. Battle, D. J. Gallon, J. Sloan, C. P. Grey, and M. J. Rosseinsky, J. Am. Chem. Soc. **124**, 620 (2002).
[20] M. M. Altarawneh, C. H. Mielke, and J. S. Brooks, Rev. Sci. Instrum. **80**, 066104 (2009).
[21] S. Ghannadzadeh, M. Coak, I. Franke, P. A. Goddard, J. Singleton, and J. L. Manson, Rev. Sci. Instrum. **82**, 113902 (2011).
[22] S. Ghannadzadeh, J. D. Wright, F. R. Foronda, S. J. Blundell, S. J. Clarke, and P. A. Goddard, Phys. Rev. B **89**, 054502 (2014).

[23] S. J. Blundell, Contemp. Phys. **40**, 175 (1999).
[24] V. Fesenko, V. Gorbunov, and V. Smilga, Physica C **176**, 551 (1991).
[25] F. Hunte, J. Jaroszynski, A. Gurevich, D. Larbalestier, R. Jin, A. Sefat, M. A. McGuire, B. C. Sales, D. K. Christen, and D. Mandrus, Nature (London) **453**, 903 (2008).
[26] M. Kano, Y. Kohama, D. Graf, F. Balakirev, A. S. Sefat, M. A. Mcguire, B. C. Sales, D. Mandrus, and S. W. Tozer, J. Phys. Soc. Jpn. **78**, 084719 (2009).
[27] M. L. Amigó, V. A. Crivillero, D. G. Franco, and G. Nieva, J. Phys.: Conf. Ser. **568**, 022005 (2014).
[28] N. R. Werthamer, E. Helfand, and P. C. Hohenberg, Phys. Rev. **147**, 295 (1966).
[29] A. Gurevich, Physica C **456**, 160 (2007).
[30] A. Gurevich, Phys. Rev. B **67**, 184515 (2003).
[31] Y. J. Uemura, G. M. Luke, B. J. Sternlieb, J. H. Brewer, J. F. Carolan, W. N. Hardy, R. Kadono, J. R. Kempton, R. F. Kiefl, S. R. Kreitzman, P. Mulhern, T. M. Riseman, D. L. Williams, B. X. Yang, S. Uchida, H. Takagi, J. Gopalakrishnan, A. W. Sleight, M. A. Subramanian, C. L. Chien, M. Z. Cieplak, G. Xiao, V. Y. Lee, B. W. Statt, C. E. Stronach, W. J. Kossler, and X. H. Yu, Phys. Rev. Lett. **62**, 2317 (1989).
[32] Y. J. Uemura, L. P. Le, G. M. Luke, B. J. Sternlieb, W. D. Wu, J. H. Brewer, T. M. Riseman, C. L. Seaman, M. B. Maple, M. Ishikawa, D. G. Hinks, J. D. Jorgensen, G. Saito, and H. Yamochi, Phys. Rev. Lett. **66**, 2665 (1991).
[33] C. Niedermayer, C. Bernhard, U. Binninger, H. Glückler, J. L. Tallon, E. J. Ansaldo, and J. I. Budnick, Phys. Rev. Lett. **71**, 1764 (1993).
[34] J. L. Tallon, J. W. Loram, J. R. Cooper, C. Panagopoulos, and C. Bernhard, Phys. Rev. B **68**, 180501 (2003).
[35] C. Homes, S. Dordevic, M. Strongin, D. Bonn, R. Liang, W. Hardy, S. Komiya, Y. Ando, G. Yu, N. Kaneko *et al.*, Nature (London) **430**, 539 (2004).
[36] F. L. Pratt and S. J. Blundell, Phys. Rev. Lett. **94**, 097006 (2005).
[37] J. L. Tallon, J. R. Cooper, S. H. Naqib, and J. W. Loram, Phys. Rev. B **73**, 180504 (2006).
[38] B. J. Taylor and M. B. Maple, Phys. Rev. B **76**, 184512 (2007).
[39] C. C. Homes, B. P. Clayman, J. L. Peng, and R. L. Greene, Phys. Rev. B **56**, 5525 (1997).
[40] A. Shengelaya, R. Khasanov, D. G. Eshchenko, D. Di Castro, I. M. Savić, M. S. Park, K. H. Kim, S.-I. Lee, K. A. Müller, and H. Keller, Phys. Rev. Lett. **94**, 127001 (2005).
[41] F. L. Pratt, P. J. Baker, S. J. Blundell, T. Lancaster, H. J. Lewtas, P. Adamson, M. J. Pitcher, D. R. Parker, and S. J. Clarke, Phys. Rev. B **79**, 052508 (2009).
[42] M. J. Pitcher, T. Lancaster, J. D. Wright, I. Franke, A. J. Steele, P. J. Baker, F. L. Pratt, W. T. Thomas, D. R. Parker, S. J. Blundell, and S. J. Clarke, J. Am. Chem. Soc. **132**, 10467 (2010).